Scatterometer Backscatter Imaging Using Backus–Gilbert Inversion

David G. Long, *Fellow, IEEE*

***Abstract*— Wind scatterometer measurements are collected over an irregular grid, and processing is required to generate backscatter images on an Earth-centered grid. The most common algorithms used for this are "drop in the bucket" (DIB) and variations of the scatterometer image reconstruction (SIR) algorithm. These algorithms are also used for radiometer brightness temperature imaging. The Backus–Gilbert (BG) algorithm has been used for radiometer imaging but has not been applied to scatterometer backscatter imaging. In this paper, the application of BG to scatterometer backscatter imaging is explored and its performance is compared to DIB and SIR. Like SIR, optimally tuned BG is capable of producing higher resolution images than DIB, though its noise performance is slightly inferior to SIR's. While BG and SIR produce similar results for radiometer data, the higher relative noise level of scatterometer data increases the differences between the SIR and BG algorithm performance, and limits the performance of BG relative to SIR in scatterometer imaging. Comparison of the SIR and BG algorithms in scatterometer imaging offers important insights into the inversion/reconstruction problem.**

***Index Terms*— Backscatter, Backus–Gilbert (BG), reconstruction, sampling, scatterometer, scatterometer image reconstruction (SIR), variable aperture.**

I. Introduction

MICROWAVE wind scatterometers measure the normalized radar cross section (σ^o) of the Earth's surface from which the near-surface wind over the ocean can be estimated. Originally designed for ocean wind estimation, wind scatterometer σ^o observations have proven useful in a variety of studies of land, vegetation, and ice [1]. Algorithms for creating images of the scatterometer surface backscatter are characterized by a tradeoff between noise and spatial and temporal resolution. Conventional gridding techniques such as "drop-in-the-bucket" (DIB) gridding provide low-noise, low-resolution products, but higher spatial resolution products are possible using image reconstruction techniques such as the scatterometer image reconstruction (SIR) algorithm [2]–[4]. These algorithms are also successfully used for creating microwave brightness temperature (T_B) images from satellite radiometer data [5], [6].

Another commonly used algorithm for T_B image formation is based on Backus–Gilbert (BG) inversion [5], [7]–[14]; however, BG has not been applied to scatterometer data. The purpose of this paper is to explore the application of BG to scatterometer backscatter imaging. We focus on evaluating BG as applied to the Ku-band SeaWinds sensor on the Quick Scatterometer (QuikSCAT) [15] mission, though the results are applicable to other wind scatterometers, as well as other types of sensors. The performance of scatterometer BG is compared to DIB gridding and SIR reconstruction. Like SIR, BG provides finer resolution backscatter images than conventional DIB; however, its effective noise performance is slightly inferior to that of SIR when applied to scatterometer data. Given the similarity in performance for BG and SIR when applied to radiometer data, the difference between the algorithms' performance for scatterometer data is surprising. Using theory, simulation and actual data, we explore the reasons for this, which we find are related to the difference in the ratio of the noise variance to the dynamic range between scatterometer and radiometer measurements. This result has important implications for applying BG to resolution enhancement or resolution matching for other active microwave sensors.

This paper is organized as follows. After some brief background, a review of SIR is provided. Simulation is then employed to compare and contrast the performance of the algorithms. Finally, a summary conclusion is provided.

II. Background

The conventional-resolution scatterometer backscatter images are based on classic DIB methods described in more detail in Section V. Enhanced-resolution products with finer spatial resolution are produced using the SIR algorithm [3], [19]. SIR uses signal reconstruction techniques to estimate σ^o on a finer grid than with simple DIB techniques. The higher resolution is possible using the measurement spatial response function (MRF) of the individual measurements. The BG algorithm offers an alternative to the use of SIR.

In this paper, SeaWinds on QuikSCAT (hereafter, QuikSCAT) data is used to compare BG and SIR algorithm performance. QuikSCAT was launched in 1999 and operated for approximately 10 years in wind observation mode. Since the failure of its spin bearing in November 2009, it has continued to collect narrow-swath data to the present. A detailed description of QuikSCAT is provided in [16]. QuikSCAT collects measurements of the surface normalized radar cross section (σ^o) at Ku-band using a dual-beam scanning pencil-beam antenna. The antenna footprint is a 25 km × 35 km ellipse on the surface. Transmit signal modulation and

Manuscript received August 4, 2018; revised October 13, 2018; accepted November 8, 2018. Date of publication December 7, 2018; date of current version May 28, 2019.

The author is with the Electrical and Computer Engineering Department, Brigham Young University, Provo, UT 84602, USA (e-mail: long@ee.byu.edu).

Color versions of one or more of the figures in this paper are available online at http://ieeexplore.ieee.org.

Digital Object Identifier 10.1109/TGRS.2018.2882136

receiver processing enables "slicing" of the footprint into finer resolution σ^o measurements [15]. Note that the measurement incidence angle over the antenna pattern 3-dB footprint varies by less than 1°. This variation is not considered in this paper.

III. Active Versus Passive Measurements

In order to understand the differences in the performance of the BG and SIR algorithms when applied to scatterometer and radiometer measurements, it is helpful to review the differences between active (radar scatterometer) and passive (radiometer) microwave measurements. Radiometer $\mathrm{T_B}$ measurements are expressed in degrees Kelvin. Over land and ice, observed $\mathrm{T_B}$ values typically range from about 220 to 290 K. Unitless scatterometer normalized radar cross section (σ^o) measurements are typically expressed in decibel and range from −40 to −5 dB at Ku-band. The measurement noise characteristics of radiometers and scatterometers are quite different. In particular, while the variability or noise in radiometer $\mathrm{T_B}$ measurements can be treated as independent of the true $\mathrm{T_B}$ value, scatterometer σ^o noise is not independent of the σ^o value [17]. In addition, the MRFs of the measurements differ. In this section, after considering the MRFs of the sensors, the different measurement noise characteristics are discussed.

A. Microwave Sensor MRFs

The effective MRF of a microwave measurement is determined by a combination of the antenna gain pattern, the observation geometry, and signal processing [1], [6], [18]. In the case of an active sensor such as a scatterometer, since the time traveled during the transmit pulselength is typically short compared to the footprint, the motion of the spacecraft during the transmit pulse can be neglected when computing the MRF, i.e., the "stop-and-hop" approximation can be applied [1]. For a passive microwave sensor, the MRF of a radiometer measurement includes the effect of antenna gain pattern smearing during the relatively long integration period [6]. In both cases, the MRF can differ from pulse to pulse, which can preclude the use of conventional image deconvolution methods.

The scatterometer-observed backscatter is related to the antenna pattern and signal processing via the integral form of the radar equation [1]. For our purposes, the measured radar echo power P_i for a particular measurement i with a particular polarization can be written in terms of ground coordinates (x, y) as

$$\mathrm{P_i} = \frac{\mathrm{P_T}\lambda}{(4\pi)^3} \iint \frac{\mathrm{G_t}(x, y; i)\mathrm{G_r}(x, y; i)\mathrm{G_p}(x, y; i)\sigma^o(x, y)}{R^4(x, y)}\, dx\, dy + \text{noise} \quad (1)$$

where $\mathrm{P_T}$ is the transmit power, λ is the radar wavelength, $\mathrm{G_t}(x, y; i)$ and $\mathrm{G_r}(x, y; i)$ are the effective transmit and receive antenna gain at the surface for the particular antenna rotation angle of the ith measurement, $\mathrm{G_p}(x, y; i)$ is the processor gain at (x, y), $R(x, y)$ is the slant range from the radar to the surface at (x, y), and $\sigma^o(x, y)$ is the normalized radar cross section. The integration is over the region of the nonnegligible gain product $\mathrm{G_t G_r G_p}$. In practice, a separate measurement of the noise-only power is made and subtracted from the measured receive signal power to estimate the signal-only power [1], [15]. The reported backscatter measurement s_i is [16]

$$s_i = \frac{\mathrm{P}_i}{X(i)} + \text{residual noise} \quad (2)$$

where the residual noise is the residual variability after noise subtraction and where the so-called "X-factor" X [18] is given by

$$X(i) = \frac{\mathrm{P_T}\lambda}{(4\pi)^3} \iint \frac{\mathrm{G_t}(x, y; i)\mathrm{G_r}(x, y; i)\mathrm{G_p}(x, y; i)}{R^4(x, y)}\, dx\, dy. \quad (3)$$

The σ^o measurement s_i can thus be modeled as

$$s_i = \iint \mathrm{MRF}_s(x, y; i)\sigma^o(x, y)\, dx\, dy + \text{residual noise} \quad (4)$$

where $\mathrm{MRF}_s(x, y; i)$ is the MRF of the particular σ^o measurement given by

$$\mathrm{MRF}_s(x, y; i) = \frac{\mathrm{P_T}\lambda}{X(i)(4\pi)^3} \frac{\mathrm{G_t}(x, y; i)\mathrm{G_r}(x, y; i)\mathrm{G_p}(x, y; i)}{R^4(x, y)}. \quad (5)$$

Noting that $R(x, y)$ is very large and varies only slightly over the nonnegligible integrand in (3), the MRF can be approximated as

$$\mathrm{MRF}_s(x, y; i) \approx C(i)\mathrm{G_t}(x, y; i)\mathrm{G_r}(x, y; i)\mathrm{G_p}(x, y; i) \quad (6)$$

where $C(i)$ is a measurement-dependent constant, that is,

$$C(i) = \frac{\mathrm{P_T}\lambda}{X(i)(4\pi)^3\overline{R}^4(i)} \quad (7)$$

where $\overline{R}(i)$ is the nominal slant range to the footprint center. The MRF is thus seen to be a function of the two-way antenna gain pattern and the processor gain function.

Note that the shape and 3-dB footprint size of the MRF differs from measurement to measurement. The nominal "resolution" of the σ^o measurement corresponds to the dimensions of the 3-dB response pattern of the MRF on the surface. This is the resolution used for conventional DIB backscatter imaging [2]; however, finer resolution backscatter images can be produced using reconstruction processing [2], [3], [19], [20].

By comparison, a particular brightness temperature measurement T_i collected by a radiometer can be written as [6]

$$T_i = \iint \mathrm{MRF}_r(x, y; i)\mathrm{T_B}(x, y)\, dx\, dy + \text{residual noise} \quad (8)$$

where $T_B(x, y)$ is the surface $\mathrm{T_B}$ and the radiometer MRF is

$$\mathrm{MRF}_r(x, y; i) = \frac{1}{G_b(i)} \int G_s(x, y; i)\, dt \quad (9)$$

where the integral is over the measurement integration period, $G_s(x, y; i)$ is the one-way antenna gain at a particular azimuth angle corresponding to the ith measurement, and

$$G_b(i) = \iiint G_s(x, y; i)\, dx\, dy\, dt. \quad (10)$$

Note that rotation of the antenna during the integration period in (9) smooths or smears the antenna pattern used in the MRF.

The key differences between the scatterometer and radiometer MRFs are: 1) the two-way antenna gain for the active sensor versus the smeared one-way gain for the passive sensor and 2) the processor gain response in the active sensor MRF. The latter enables radar to use Doppler and range processing to achieve finer resolution than the antenna pattern alone, whereas the one-way antenna pattern and the measurement integration dictate the radiometer measurement resolution. As a result, scatterometers can have much finer (6 km × 15 km) spatial resolution (i.e., more localized MRFs) than radiometers (25 km × 25 km or larger depending on frequency). Another difference is in the selection of the antenna gain pattern: radiometers choose antenna patterns with very low sidelobes, whereas radars typically emphasize minimum mainlobe width at the expense of higher sidelobes. Higher sidelobes enable better resolution enhancement in reconstruction [3].

IV. Measurement Noise in Scatterometer and Radiometer Measurements

Radiometric noise due to thermal noise in the receiver affects both active and passive measurements. Measurement variability also arises due to signal variability. In radiometers, the net measurement variability is quantified by its standard deviation given by $\Delta T = \sqrt{\mathrm{Var}(T_i)}$, which is inversely proportional to the square root of the time-bandwidth product. ΔT is known as the "radiometric resolution" [1]. The residual noise in (8) can be modeled as additive white noise with a standard deviation of ΔT. For satellite radiometers, ΔT is no more than a few Kelvin, and is typically 1 K or less. For a given mean $\mathrm{T_B}$, the "normalized radiometric resolution" is $K_r = \Delta T/T_B$, and is of order 0.004 for a modern radiometer observing land. The normalized radiometric resolution K_r for a radiometer is similar to scatterometer K_p.

In addition to radiometric (thermal) noise, scatterometer measurements also include signal variability (which is also considered "noise") due to coherent signal effects, such as speckle and Raleigh fading or scintillation. These result in undesired variability in the measurement that is correlated with the desired signal. The total variability of scatterometer measurements is quantified by the normalized measurement standard deviation K_p [17], [23], [24]

$$K_p = \frac{\sqrt{\mathrm{Var}(s_i)}}{\mathrm{mean}(s_i)}. \tag{11}$$

The scatterometer K_p gives the normalized radiometric resolution of the sensor. For most scatterometers [1], [17], K_p^2 can be written as a quadratic function of the measurement signal-to-noise ratio (SNR)

$$K_p^2(\mathrm{SNR}) \approx \frac{1}{B_s T_G}\left(1 + \frac{2}{\mathrm{SNR}} + \frac{1}{\mathrm{SNR}^2}\right) \tag{12}$$

where B_s is the measurement bandwidth and T_G is transmit pulselength. The noise model for a measurement z_i of a particular true s_i can be written as

$$z_i = s_i(1 + K_p \nu_i) \tag{13}$$

where ν_i is an independent, unit-variance, and zero-mean Gaussian random variable [2].

For QuikSCAT, K_p varies from 0.02 to as high as 3, though the nominal QuikSCAT K_p is of order 0.05. Comparing this value of scatterometer K_p to the normalized radiometric resolution for a typical radiometer, we observe that scatterometer measurements ($K_p = 0.05$) are proportionally much noisier than typical radiometer measurements ($K_r = 0.004$). This difference is important when comparing the relative performance of different imaging algorithms when used for different types of sensors.

Note that due to the relatively high measurement noise in scatterometer σ^o measurements, the reported σ^o measurements can occasionally be negative. This can produce negative pixel values unless the nonphysical negative σ^o measurement values are discarded. Unfortunately, discarding negative σ^o measurements can introduce an estimate bias. Fortunately, negative σ^o measurements only rarely occur over land and ice and so are discarded for this paper. The possible bias effect is not considered in this paper. Radiometer measurements are always positive and there is a large offset from zero in the brightness temperature measurements so negative measurements do not occur.

V. Imaging

To generate σ^o or $\mathrm{T_B}$ images from the sensor measurements, the measurements collected over one or more passes of the study area may be combined. Combining passes increases the effective sampling density, which enables finer resolution reconstruction. Note that while the image is produced on a regularly spaced earth-centered grid, the individual measurement locations are on an irregular sampling pattern relative to the grid. Longer discussions on this are provided in [2] and [6].

A simple σ^o or $\mathrm{T_B}$ image map can be created by merely gridding the data based on location and averaging all measurements whose centers fall into the same map pixel grid element, i.e., DIB gridding. DIB has the advantage of not requiring any information about the MRF. Conventional DIB should use a grid size compatible to the 3-dB footprint size [2]. To produce finer resolution images, reconstruction techniques, which employ both the measurement locations and the MRFs of the measurements, can be employed.

When discretized on the imaging grid and ignoring noise, the measurement equation [(4) for σ^o and (8) for $\mathrm{T_B}$] can be expressed as [2], [6]

$$z_i = \sum_{j \in \mathrm{image}} h_{ij} a_j \tag{14}$$

where h_{ij} is the discretely sampled MRF for the ith measurement evaluated at the jth pixel center and a_j is the backscatter or $\mathrm{T_B}$ value for the jth pixel. Here, for convenience, h_{ij} is normalized so that $\sum_j h_{ij} = 1$. In practice, the MRF is negligible some distance from the measurement center, so the sums need only be computed over a small area around the pixel. Equation (14) can be written as the matrix equation

$$\vec{Z} = \mathbf{H}\vec{a} \tag{15}$$

where $\mathbf{H}$ contains the sampled MRF for each measurement and $\vec{Z}$ and $\vec{a}$ are vectors composed of the measurements z_i and the pixel values a_j, respectively. Estimation (reconstruction) of the surface σ^o or T_B is equivalent to inverting (15). To minimize the effects of noise, the inversion may be only partial, i.e., a regularized solution [2], [6].

A. SIR

The iterative SIR algorithm [2], [3], [19] was developed specifically for scatterometer image formation and is a particular implementation of an iterative solution to (15). SIR approximates a maximum-entropy solution to an underdetermined equation and a least-squares solution to an overdetermined system. The first iteration of SIR, termed "AVE" (for weighted AVErage) [19], is often used in enhanced resolution scatterometer wind retrieval [21], [22]. The AVE estimate of the jth pixel is given by [19]

$$a_j = \frac{\sum_i h_{ij} z_i}{\sum_i h_{ij}} \tag{16}$$

where the sums are over all measurements that have nonnegligible MRF at the pixel. The SIR iteration begins with an initial image a_j^0 whose pixels are set to be the AVE value defined in (16). Thereafter, the SIR algorithm iteratively updates the backscatter image estimate. At the kth ($k > 0$) iteration of SIR, the jth image pixel a_j^k is computed using [3]

$$\begin{aligned}
f_i^k &= \frac{\sum_n h_{in} a_n^k}{\sum_n h_{in}} \\
d_i^k &= \sqrt{z_i / f_i^k} \\
u_{i,j}^k &= \begin{cases} \left[\dfrac{1}{2 f_i^k}\left(1 - \dfrac{1}{d_i^k}\right) + \dfrac{1}{a_j^k d_i^k}\right]^{-1}, & d_k^k \geq 1 \\ \left[\dfrac{1}{2} f_i^k (1 - d_i^k) + a_j^k d_i^k\right], & d_k^k < 1 \end{cases} \\
a_j^{k+1} &= \frac{\sum_i h_{ij} u_{i,j}^k}{\sum_i h_{ij}}.
\end{aligned}$$

The iteration continues until convergence. While each iteration improves the signal reconstruction error, it also increases the noise [2]. The number of SIR iterations thus plays a noise-signal tradeoff role similar to the BG γ parameter described in the following.

For scatterometers, SIR has traditionally been implemented in decibel; i.e., the computation is done on $z_i = 10 \log_1(s_i)$ rather than on the linear-space value[1] or $z_i = s_i$. The resulting images are in decibel. This approach is used in this paper. Comparison with linear computation shows that computation in decibel produces more accurate images by reducing the effects of noise [2]. For T_B imaging, computation is done in linear space in the radiometer version of the SIR algorithm so a_j and z_i are in Kelvin [6].

[1]Note that σ^o is a fundamentally unit-less quantity defined as the ratio of two areas [1].

B. Backus–Gilbert

The BG inversion method [7], [8] provides an alternate approach to inverting (4) based on least squares [11]. Successfully used for radiometer data, BG has not previously been applied to scatterometer data. The essential idea is to estimate the surface backscatter at a given pixel from a weighted linear sum of the measurements collected "close" to the pixel, that is,

$$\widehat{a}_j = \sum_{i \in \text{nearby}} w_{ij} z_i \tag{17}$$

where the sum is computed over nearby pixels and with the weights w_{ij} selected to sum to one, i.e., $\sum_i w_{ij} = 1$. To derive the weights w_{ij} for a particular pixel j, the total squared error is minimized. The reconstruction error $e_j = \widehat{a}_j - a_j$ for the jth pixel is then the sum of the signal reconstruction error s_j and noise reconstruction error n_j, derived as follows:

$$\begin{aligned}
e_j = \widehat{a}_j - a_j &= \sum_{i \in \text{nearby}} w_{ij} z_i - a_j && (18) \\
&= \left(\sum_{i \in \text{nearby}} w_{ij} \sum_k h_{ik} a_k + \sum_{i \in \text{nearby}} w_{ij} \text{noise}_i \right) - a_j && (19) \\
&= s_j - n_j && (20)
\end{aligned}$$

where

$$s_j = \sum_{i \in \text{nearby}} w_{ij} \sum_k h_{ik} a_k - a_j \tag{21}$$

$$n_j = \sum_{i \in \text{nearby}} w_{ij} \text{noise}_i. \tag{22}$$

Following the weighted metric approach of [9], we consider the case of a unit delta function centered at $a_j = 1$, so that $a_k = 0$ for all $k \neq j$. The signal reconstruction error can then be written as

$$s_j = \sum_{i \in \text{nearby}} w_{ij} h_{ik} - 1. \tag{23}$$

The squared image reconstruction error $Q_R = s_j^2$ is then

$$Q_R = \left(\sum_{i \in \text{nearby}} w_{ij} h_{ij} - 1 \right)^2 \tag{24}$$

while the squared noise error $Q_N = n_j^2$ is given by

$$Q_N = \left(\sum_{i \in \text{nearby}} \sum_{l \in \text{nearby}} w_{ij} w_{lj} n_i n_l \right). \tag{25}$$

Taking the expectation of the noise product, Q_N can be expressed as

$$Q_N = \vec{w}^T \mathbf{E} \vec{w} \tag{26}$$

where $\vec{w}$ with elements $(\vec{w})_i = w_{ij}$ is the vector of the weights w_{ij} for the jth pixel and $\mathbf{E}$ is the measurement noise covariance matrix. Typically, the noise is assumed to be spatially uncorrelated. This assumption is not generally true for scatterometer measurements [17] but it makes the analysis and computation simpler. Then, $\mathbf{E}$ is a diagonal matrix with diagonal entries σ_n^2, where σ_n is the measurement noise standard deviation, that is,

$$\mathbf{E} = \sigma_n^2 \mathbf{I}. \tag{27}$$

To provide a tradeoff between noise and resolution in the BG reconstruction, Backus and Gilbert [8] introduced the tuning parameter γ to weight the signal reconstruction error ($\mathrm{Q_R}$) and the noise error ($\mathrm{Q_N}$) in the total error Q, that is,

$$Q = \mathrm{Q_R}\cos\gamma + \omega \mathrm{Q_N}\sin\gamma \tag{28}$$

where ω is a dimensional tuning parameter included to ensure compatibility of the signal and noise terms [9]. As derived by Backus and Gilbert [8] and expressed in discrete form, the total error Q is minimized when the weight vector for the pixel is selected as[2]

$$\vec{w} = \mathbf{Z}^{-1}\left(\vec{v}\cos\gamma + \frac{1 - \vec{u}^T\mathbf{Z}^{-1}\vec{v}\cos\gamma}{\vec{u}^T\mathbf{Z}^{-1}\vec{u}}\vec{u}\right) \tag{29}$$

where

$$\mathbf{Z} = \mathbf{G}\cos\gamma + \omega\mathbf{E}\sin\gamma \tag{30}$$

with the elements of the vectors and matrices defined as

$$\begin{aligned}(\vec{u})_i &= 1\\ (\vec{v})_i &= h_{ij}\\ \mathbf{G}_{ik} &= \sum_{n\in\mathrm{nearby}} h_{in}h_{kn}.\end{aligned}$$

As noted, the BG approach has two tuning parameters: the arbitrary dimensional parameter ω and the noise-tuning parameter γ: ω ensures that $\mathrm{Q_R}$ and $\mathrm{Q_N}$ are on compatible scales, while γ controls the tradeoff between noise and signal reconstruction accuracy. Ideally, ω is chosen so that the variation of the total error falls at a middle value of γ, which can vary from 0 to $\pi/2$ [8]. The γ parameter affects the spatial resolution of the results. Varying γ alters the solution for the weights between a (local) pure least-squares solution and a minimum noise solution. The value of γ must be selected subjectively to "optimize" the resulting image and depends on the measurement noise standard deviation [11]. Selection of $\gamma = \gamma'\pi/2$ is discussed in more detail later. Like SIR, BG can be computed in decibel or normal space, and the results are similar. Note that while SIR makes no assumptions about the distribution of the noise, BG requires knowledge of the noise variance and implicitly treats the noise as Gaussian distributed. We note that using values in decibel tends to correlate the signal and noise, and makes the noise distribution non-Gaussian.

To ensure tractable computation, the weights for each pixel are computed separately using only "nearby" measurements, here defined to be the region where the individual measurement MRF evaluated at the pixel center is within 10 dB of the peak response. Nevertheless, the computation requirements of the BG method can be very intensive compared to SIR since each pixel requires a matrix inversion [6].

[2]A typographical error is present in this expression in [11].

VI. Image Formation Performance Simulation

To analyze the performance of the BG reconstruction, it is helpful to use simulation where the true image is known. The results of these simulations inform the tradeoffs in applying the algorithm and understanding its limitations. The simulation (described in more detail in [2]) uses the actual locations, geometry, and MRFs of real QuikSCAT "slice" measurements extracted and computed from QuikSCAT Level-1B files [16]. A synthetic "truth" image is first created, and simulated noisy and noise-free measurements are created using the locations and computed MRFs. From the measurements, BG and SIR images are created, with error metrics mean and rms determined for each case. This process is repeated separately for each QuikSCAT polarization, though only a single polarization is shown. Monte Carlo noise is included in the measurements using the noise model (13) with the average system K_p estimated from the actual measurements. The average noise variance σ_n^2 is then

$$\sigma_n^2 = \langle s_i^2 K_p^2\rangle. \tag{31}$$

The reconstructed images are computed on a fine-resolution 2.225-km grid, which well oversamples the 3-dB QuikSCAT slice footprint size of approximately 6 km $\times$ 25 km. For example, simulation results are shown in Fig. 2. In later figures, the effects of varying the values of ω and σ_n are considered. For comparison with the BG results, SIR, AVE, and DIB images are also created. Simulated DIB images are created by collecting and averaging all measurements whose centers fall within each low-resolution (22.25 km, 10 times the fine resolution dimension) grid element. When preparing DIB images for display, the coarse DIB resolution image is pixel replicated to match the pixels of the fine-resolution images. Error statistics (mean m_{err}, standard deviation s_{err}, and rms) are computed from the difference between the truth and estimated images for each algorithm, that is,

$$m_{\mathrm{err}} = \langle \mathrm{est}_k - \mathrm{true}_k\rangle \tag{32}$$

$$s_{\mathrm{err}} = \sqrt{\langle(\mathrm{est}_k - \mathrm{true}_k)^2\rangle - m_{\mathrm{err}}^2} \tag{33}$$

where est_k and true_k are the kth pixel in the estimated and true images, respectively.

The arbitrary "truth" image is generated with representative features including spots of varying sizes, edges, and areas of constant and gradient backscatter (Fig. 2). We note that the optimum values of the various algorithms parameters can depend somewhat on the truth image used [3], [4]; however, for clarity the results from only a single truth image are presented in this paper. The overall conclusions apply to other images. In the simulation, the azimuth and incidence angle dependence of σ^o is ignored.

In doing this analysis, we recall that the value of noise standard deviation (σ_n) is determined by the sensor (via the K_p parameters) and the scene σ^o, and thus may vary. Thus, performance for various values of σ_n is considered. Since the value of the scaling parameter ω is somewhat arbitrary [12], the peformance of the algorithm for different ω is also considered, with performance optimized as a function of the BG tuning parameter γ. Since the product $\gamma\omega$ is multiplied by

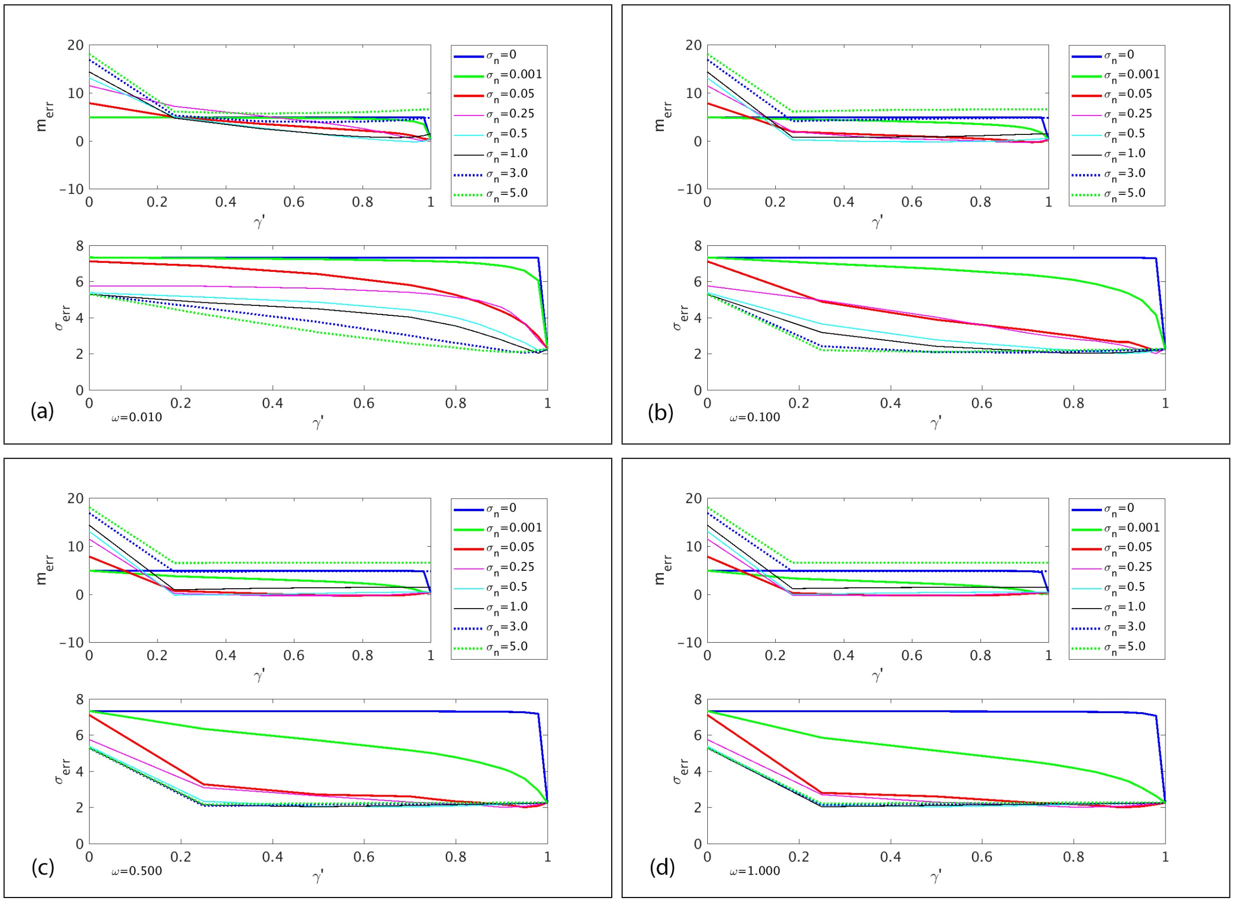

Fig. 1. BG simulation mean and standardard deviation results for various σ_n, γ' values, and ω values. (a) $\omega = 0.01$. (b) $\omega = 0.1$. (c) $\omega = 0.5$. (d) $\omega = 1$. See text. The value of ω effects where the minimum σ_{err} occurs but has little impact on the actual minimum value.

σ_n^2 in the BG algorithm, the values of these parameters are conflated when analyzing the BG performance.

To select the optimum γ, images for different γ values are computed. The reconstruction error versus γ' for these images is shown in Fig. 1, with the images shown in Fig. 2. At small γ', the image exhibits significant overshoot and texturing. As γ' is increased, the image becomes smoother and subjectively less sharp. Comparing the image panels in Fig. 2, it becomes apparent that choosing an optimum value of γ' is important for BG to prevent excessive "ringing" artifacts or over smoothing. The BG images for $\gamma' \geq 0.5$ are visually similar to the SIR result, with progressively more smoothing as γ' is increased. For further insight, Fig. 3 plots horizontal lines extracted through one of the spot features in the panes in Fig. 2.

VII. Analysis

The BG method has proven to work well with radiometer data [6] where the nominal measurements values range from 160 to 230 K with a standard deviation of order 1.0–0.5 K. Thus, K_r is a fraction of a percent. The effective image "SNR" is thus uniformly very high, ∼23–26 dB, while the dynamic range is small (a few decibel[3] at most). In contrast, QuikSCAT land/ice scatterometer measurements have a much wider dynamic range with σ^o values from −30 to 0 dB, and overall lower SNR values, varying from −10 to 20 dB with nominal K_p close to 0.05. Thus, scatterometer measurements are proportionally much noisier than the radiometer measurements. The higher K_p leads to lower performance of BG for scatterometer data, as well as the need for different tuning of γ' for scatterometer data compared to radiometer data with its lower K_r.

In this paper, BG is computed in linear space (not in decibel), with the resulting images converted to decibel for display. A distinct disadvantage of linear-space BG is that it can produce negative (in linear-space) σ^o image values, which are nonphysical, whereas SIR results correspond to strictly positive linear-space σ^o values. Computation of BG using decibel measurements was tested and found not to provide any performance advantage over linear-space measurements.

A. Performance Versus Noise Level

To evaluate the effects of the scatterometer noise level on the BG reconstruction performance, a wide range of scatterometer noise levels are considered, with lower noise levels corresponding to smaller σ_n and K_p values. The simulation results are presented for multiple ω values as a function of γ' in Fig. 1. These busy plots are summarized in Figs. 4 and 5.

In Fig. 1, note how the minimum error tends to shift toward the left as ω is increased. The value of ω affects where the

[3] dB(x) is defined as $10\log_{10}(x)$.

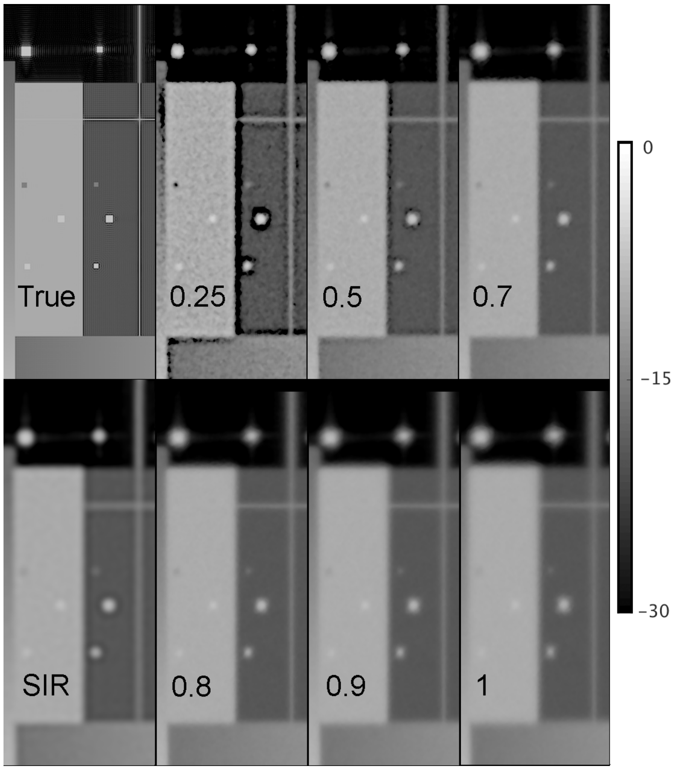

Fig. 2. Simulation results for BG with various γ' values for $\omega = 0.5$ and $\sigma_n = 0.5$ and SIR for iteration 20. (Top left) True image. (Bottom left) SIR comparison image. Other images are BG with the γ' value indicated on the image. Based on rms error minimization the "optimum" (minimum rms) γ' is at $\gamma' = 0.5$.

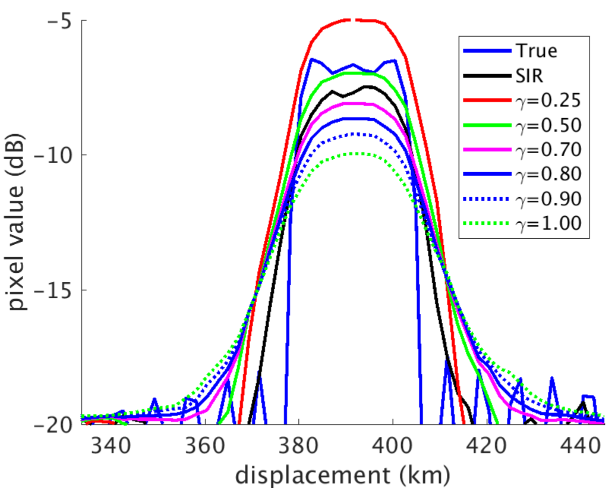

Fig. 3. Represenatitive comparison of horizontal transects for various cases through the center-right most spot feature in Fig. 2. A low BG γ the spot is wider and taller than the true. As γ is lowered, the peak undershoots the true height and the spot becomes wider. The SIR image slightly undershoots the peak but is narrower than any of the BG results.

minimum occurs but has little impact on the actual minimum error statistic. While the value of ω ideally should be chosen so that minimum error occurs in the middle of the γ' range, this is not possible to achieve for small values of σ_n. However, at larger σ_n, $\omega = 0.1$ or $\omega = 0.5$ are usable, with the latter best centering the minimum over the range values expected. From Fig. 4, note that the lowest error at the optimum γ' is roughly a linear function of σ_n. It is interesting to point out

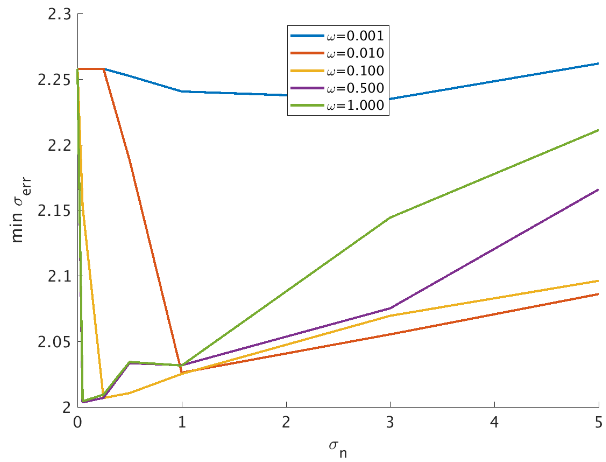

Fig. 4. Plot of the minimum error standard deviation determined over γ versus σ_n for different values of ω. The value of ω affects where the minimum occurs but has little impact on the actual minimum value for $\sigma_n > 1$.

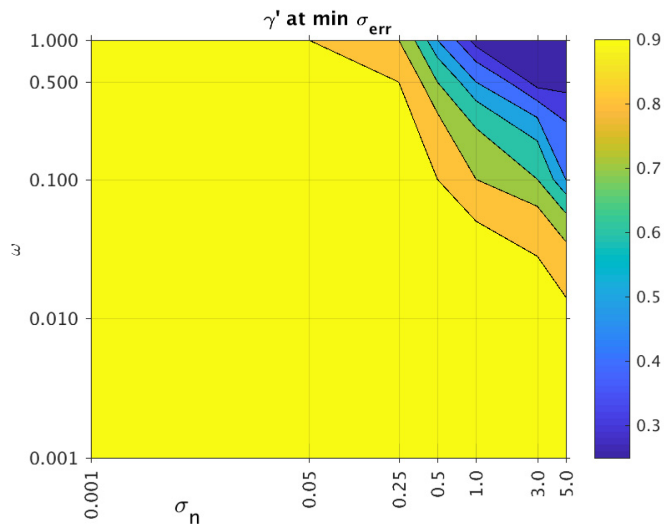

Fig. 5. Plot of the value of γ' corresponding to the location of the minimum error standard deviation versus ω and σ_n. The color scale is clipped to the range shown for visibility. (Top right) Note that γ' saturates for $\omega < 0.1$ for all σ_n values and that the optimum value of γ' is nearly a linear function of ω and σ_n.

that the error for $\sigma_n = 0$, which is effectively the signal-only reconstruction error, is larger than for $\sigma_n > 0$. This confirms that σ_n in E acts as a regularization term in the reconstruction and explains why the smallest total rms error occurs at the largest σ_n value.

Since σ_n is approximately 0.05 for QuikSCAT data, to minimize the total error a large ω value should be chosen, but because the plots at the minimum are very flat, the precise values of either ω or γ' are not critical, and round number values can be used.

B. SIR Comparison

While simulation enables evaluation of the absolute performance of BG using the truth image, the lack of truth data when using actual data precludes a simular analysis. Instead, SIR results are used as a reference to compare the BG images to. To prepare for this comparison, we first use simulated data to compare BG and SIR results.

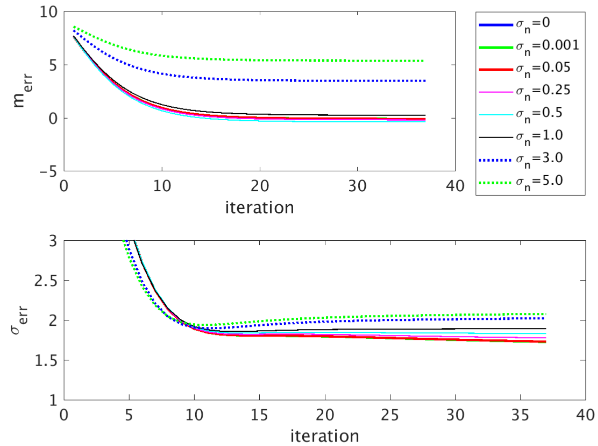

Fig. 6. (Top) mean and (Bottom) standard deviation of the SIR error versus iteration number for various σ_n values. For convenience, the iteration is truncated at a maximum of 37. For low σ_n, the error continues to decrease with increasing iterations, while at higher σ_n ($\sigma_n > 1$), the minimum error occurs for an iteration less than 37.

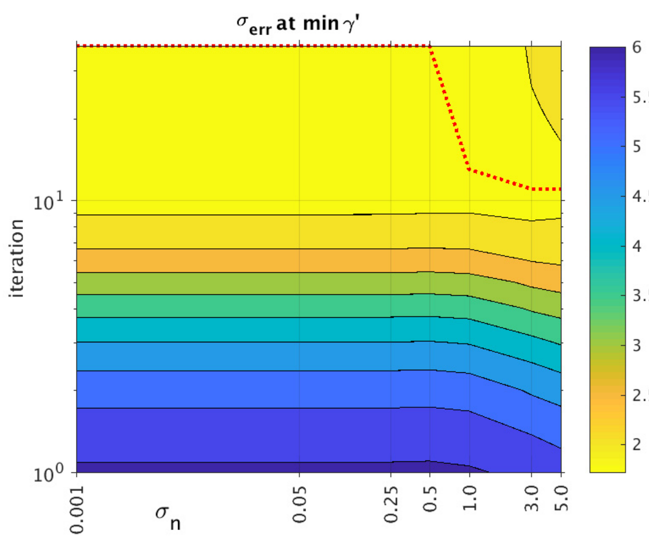

Fig. 7. Plot of the total error standard deviation versus iteration number and noise standard deviation σ_n for SIR. The iteration has been truncated to an arbitrary maximum of 37. Dotted line: location of the minimum error, which occurs at the maximum iterations for $\sigma_n < 0.5$. This suggests that for $\sigma_n < 0.5$ the reconstruction error can be reduced by further iteration than shown in this plot.

As noted previously, the number of iterations controls the noise/resolution tradeoff in SIR. Fig. 6 presents plots of the error performance versus iteration number for various values of the noise standard deviation σ_n for SIR. As has been previously demonstrated [2], the signal reconstruction error decreases with increasing iteration, while the noise error increases with increasing iteration. Thus, for a given σ_n, there is an optimum number of iterations which minimizes the total error. This is evident in Fig. 6 where the error standard deviation is minimized at 10 iterations at large σ_n. The location of the minimum is a function of the noise level that shifts to the right as the noise level is decreased, finally increasing to infinity as the noise level goes to zero. This behavior is apparent in Figs. 7 and 8 which present the error versus iteration and noise level in different forms. The optimum

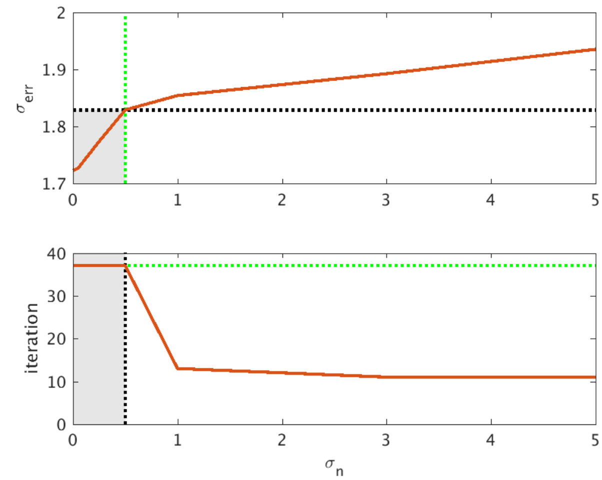

Fig. 8. (Top) Plot of the minimum error over iteration versus the noise standard deviation σ_n. The iteration has been truncated to a maximum of 37, which denoted by the dashed lines and shaded area. The error in the gray region can be reduced by further iteration. (Bottom) The iteration at which the minimum error standard deviation is reached. In these plots, the maximum number of iterations is limited to 37, which is denoted by the dashed lines and the shaded area.

number of iterations that minimizes the total error for $\sigma_n = 0.5$ is nominally approximately 37. Furthermore, iteration slowly increases the total error due to increasing noise. For this reason, the number of iterations in the comparisons is truncated at 37.

From Fig. 8, the minimum SIR rms error at $\sigma_n = 0.5$ is 1.82, which is less than the smallest achievable BG value of slightly over 2.0 from Fig. 4. This leads to the observation that SIR has less error than optimized BG for QuikSCAT backscatter imaging, i.e., SIR is more effective in noise suppression even though the resulting images are visually similar (see Fig. 2), though are not identical even in the noise-free case.

The mean m_{diff} and standard deviation σ_{diff} of the difference of the BG and SIR images are computed for various γ', σ_n, and ω values and plotted in Figs. 9 and 10. Examining the difference statistics plots, we can conclude that there is a fairly wide range of ω and σ_n values that produce essentially the same minimum difference value, and that choosing $\omega = 0.5$ enables a wide γ' tuning range that supports the expected true σ_n of 0.5. This result is confirmed in Fig. 10 which shows the difference standard deviation versus σ_n for various ω values.

VIII. Pixel Spatial Response Function

The pixel spatial response function (SRF) describes the SRF of each pixel and is effectively the impulse response function. For BG, the image backscatter value reported for each pixel is computed as the weighted sum of measurements local to the pixel [see (17)]. Due to the variation in the positions of the measurements with respect to the pixel the weights vary from pixel to pixel, i.e., the SRF is spatially varying. This precludes the use of conventional deconvolution algorithms for resolution enhancement. The 3 dB width of the SRF defines the effective resolution of the estimated image. Here, the SRF of BG is compared with the SRF of SIR.

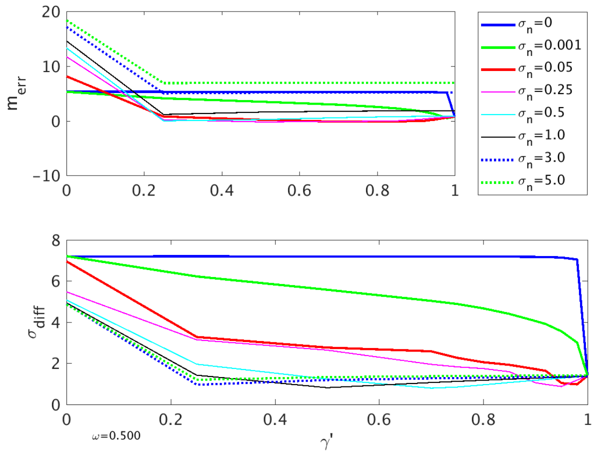

Fig. 9. Difference (BG-SIR) statistics versus γ' for various assumed noise standard deviations and γ' values for $\omega = 0.5$.

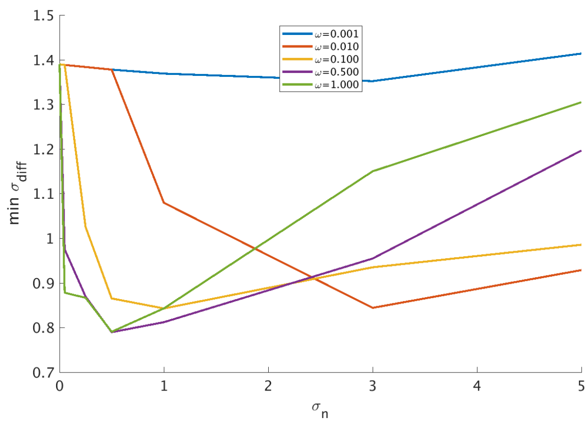

Fig. 10. Plot of the minimum difference BG-SIR standard deviation determined over γ versus σ_n for different values of ω. With an expected σ_n of 0.3–0.5 for scatterometer measurements, ω values between 0.1 to 1 help ensure the minimum error can be achieved.

The effective BG SRF can be analytically computed for each pixel. However, due to the nonlineary in SIR, the SIR SRF has to be computed numerically using simulation. In this paper, simulation is used computing the SRFs for both. A single, arbitrarily selected, pixel is set to a high σ^o value with the remaining pixels set to low, but nonzero σ^o values. The SRF is the resulting normalized image. The BG SRF versus γ' is shown in Fig. 11 where it is compared to the SIR SRF for a randomly selected pixel. Slices through the SRFs are shown in Fig. 12. The slices confirm that the SRF is not symmetric for this pixel. Note that for small γ', the SRF is potentially compact but is offset and confused. As γ' increases, the BG SRF becomes better localized but widens its region of support. This is the result of the noise regularization which "smooths" the result in order to reduce the noise. This has the side effect of degrading the signal SRF. This behavior confirms the noise and resolution tradeoff observed with the error analysis.

In comparison, the SIR SRF has lower, more compact side lobes than any of the BG results. A γ' value of 0.25–0.3 best approximate the 3 dB width of the SIR SRF. At the larger γ' values suggested by the error analysis, the 3-dB SRF resolution of the BG result is coarser than the SIR result.

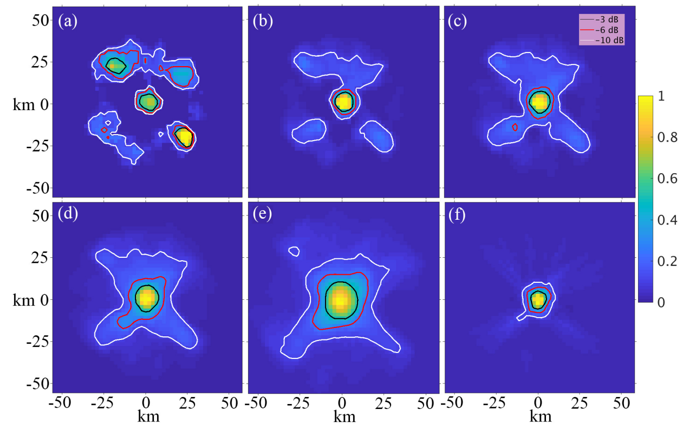

Fig. 11. Plots of the pixel SRF of an arbitrary pixel for various BG γ' values for $\omega = 0.5$ and $\sigma_n = 0.5$ compared to optimized SIR. (a) BG $\gamma' = 0$, (b) BG $\gamma' = 0.25$, (c) BG $\gamma' = 0.5$, (d) BG $\gamma' = 0.75$, (e) BG $\gamma' = 1$, and (f) SIR with 30 iterations.

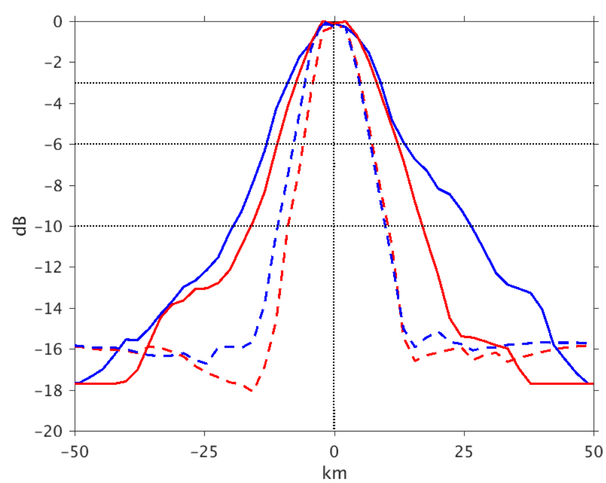

Fig. 12. Plots of x (red) and y (blue) slices through the optimized BG (solid lines) and SIR (dashed lines) SRFs. Note that the slices in different directions are slighty different to the asymmetry of the SRF. Dotted horizontal lines: at -3, -6, and -10 dB. The mean SRF -3-dB width is approximately 17.8 km for BG and 10.0 km for SIR which is the effective resolution achievable for this particular pixel.

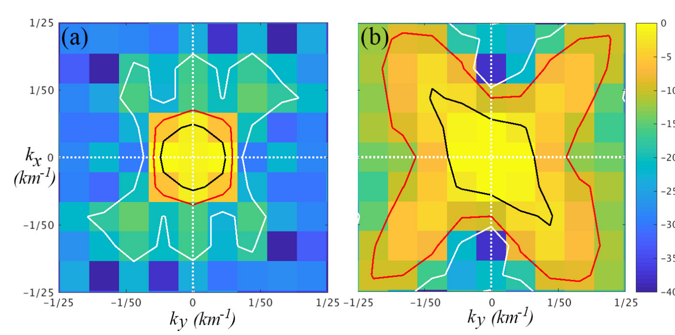

Fig. 13. Plots of the spectrum of the pixel SRF of an aribitrary pixel. (a) Optimized BG ($\gamma' = 0.5$ assuming $\sigma_n = 0.5$. (b) SIR at 37 iterations. The contour levels are at -3 dB (black), -6 dB (red), and -10 dB (white).

The spectrum of the SRF reveals information about the image resolution. Spectra of the BG and SIR SRFs are shown in Fig. 13. Note that BG SRF is compact, but the 6-dB contour is limited to spatial frequencies less than approximately 1/50.

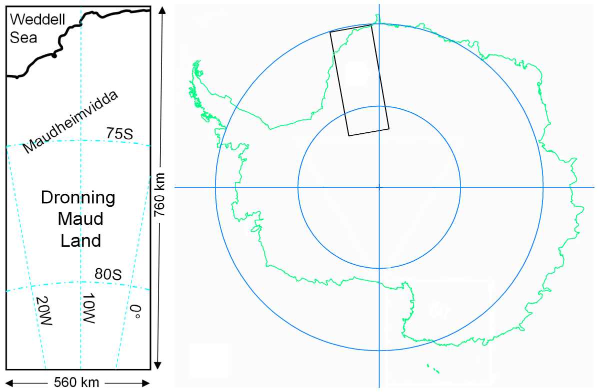

Fig. 14. Map of the location of the data study area over Antarctica.

The SIR SRF extends over a much larger area of the spectrum, which confirms its finer resolution capability even in the noise-free case. Note that while the BG SRF spectrum is roughly circular symmetric, the SIR SRF spectrum is not. This is the result of the spatial distribution of the σ^o measurements surrounding this particular pixel. The assymmetry suggests that the frequency content of the SIR image may be directionally dependent, i.e., the image spectra may also be assymmetric, whereas the BG spectrum is more symmetric.

IX. Actual Data

While the previous results are based on simulation, in this section, we compare BG and other methods using actual data. To enable detailed comparison of the algorithms for a four-day integration period, a small 580 km × 1400 km study area extending from the Antarctic coast into the interior along the prime meridian is arbitrarily selected. A location map of the study area is shown in Fig. 14. The results from applying BG with different γ' values is shown along with a SIR comparison image in Fig. 15. Because the true σ^o values are not known, error statistics cannot be computed. Instead, the mean m_{diff} and standard deviation σ_{diff} of the difference of the BG and SIR images are computed for various γ', σ_n, and ω values and plotted in Figs. 16–18. This is the same study regions used in [2], and a longer, more detailed analysis of the SIR result is provided there. Here, we emphasize the BG comparison.

As in the simulation, visual comparison of the BG images reveals significant changes in the dynamic range and sharpness of the BG image as a function of γ'. At high γ' values, the image is very smooth, while at low γ' values the image is sharper, but can also exhibit negative σ^o values. The SIR image reveals subjectively somewhat finer detail than in any of the BG cases, and so is used as the reference for the remaining analysis.

To better understand the effects of the choice of ω and the assumed σ_n value on the results using real data, Fig. 16 plots the difference statistics versus γ' for various ω and assumed σ_n values. Subjectively, the images corresponding to these values are indistinguishable. As in the simulated data case, there is a fairly wide range of ω and σ_n values that enable finding the same minimum difference value. However, the differences using the actual data are smaller than in the simulation. This may be due to the longer integration period used with the

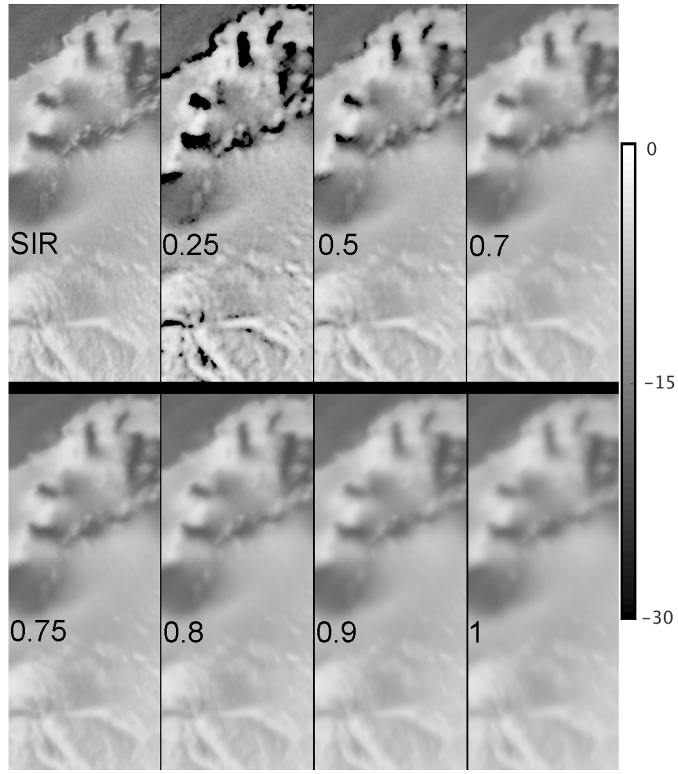

Fig. 15. QuikSCAT egg V-pol study area σ^o images created from four days (254–257, 1999) of actual data. (Top left) SIR (30 iterations) comparison image. The remaining panels are BG for different values of γ' as indicated on the image computed with $\omega = 0.5$ and $\sigma_n = 0.5$. The artifacts are extreme at low γ', with a reduction in dynamic range and increased smoothing as γ' is increased.

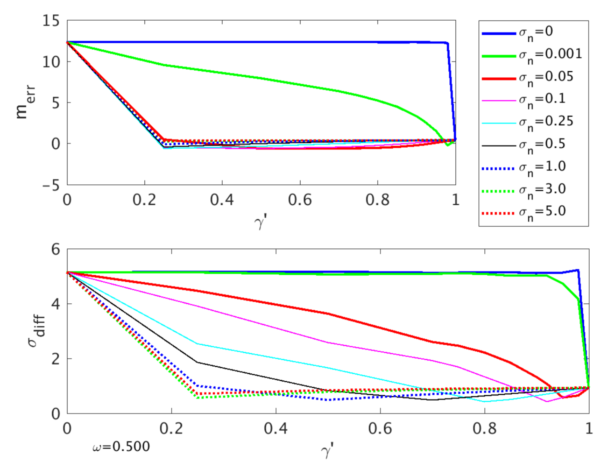

Fig. 16. Difference (BG-SIR) statistics versus γ' for various assumed noise standard deviations σ_n and γ' values for $\omega = 0.5$.

actual data. In any case, we conclude that choosing $\omega = 0.5$ enables a wide γ' tuning range that supports the expected true σ_n of 0.5, though other values can be used. This result is confirmed in Fig. 17, which shows the difference standard deviation versus σ_n for various ω values. While this plot is a little noisy, several values of ω yield near-minimum difference statistics at the expected $\sigma_n = 0.5$.

Finally, we note from Fig. 18 that the optimum γ' is roughly a linear function of ω and σ_n. At the expected $\sigma_n = 0.5$ and using $\omega = 0.5$, the optimum γ' occurs at 0.5. These choices

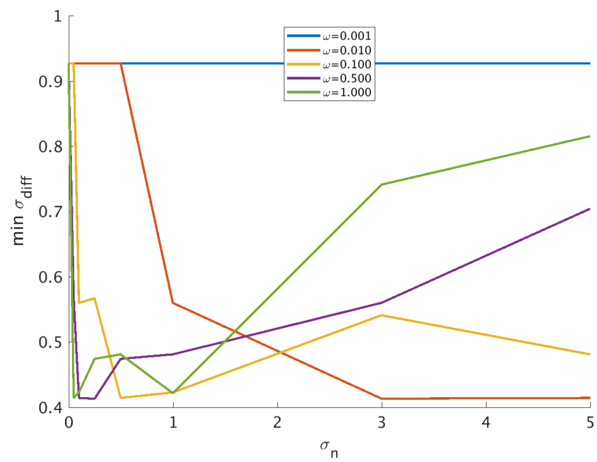

Fig. 17. Plot of the minimum difference BG-SIR standard deviation determined over γ versus σ_n for different values of ω.

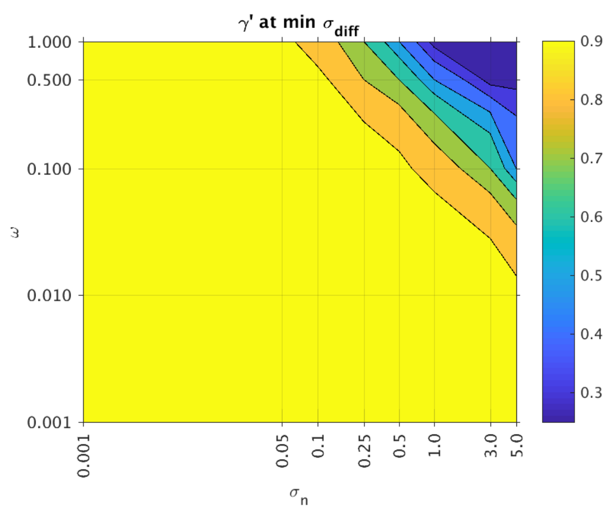

Fig. 18. Plot of the value of γ' corresponding to the location of the minimum BG-SIR difference standard deviation versus ω and σ_n. The color scale is clipped to the range shown for visibility. Note that the optimum γ' is roughly a linear function of ω and σ_n.

for σ_n and ω offer a wide tuning range for γ' to optimize image construction and provide subjectively the best quality images.

X. Conclusion

This paper has explored the application of BG to scatterometer backscatter imaging and compared the results with conventional DIB gridding and SIR imaging for SeaWinds-class scatterometers using both simulation and actual data. BG has the advantage of being linear (in the measurements) and computation of the BG weights can be done independent of the actual measurements, whereas SIR is a data-driven, nonlinear algorithm.

BG has proven very successful for radiometer data processing. In this paper, we have optimized BG for application to QuikSCAT measurements. We find it less useful for scatterometer image formation due to the effects of the lower effective K_r of scatterometer data compared to that of radiometer data. While the signal resolution enhancement for BG can be visually similar to SIR, the minimum total error standard deivation for BG is found to be somewhat inferior to SIR, which suggests that SIR is more effective at noise suppression at low SNRs. With BG optimized to minimize the error, a comparison of the resulting pixel SRF suggests that the effective resolution of BG is coarser than SIR, i.e., SIR can provide finer resolution for the same total error level. Furthermore, the intense computational requirements for BG are a limiting factor in applying it to large data sets. For these reasons, BG is not recommended for scatterometer backscatter image construction and alternate algorithms such as SIR are recommended instead.

References

[1] F. Ulaby and D. G. Long, *Microwave Radar and Radiometric Remote Sensing*. Ann Arbor, MI, USA: Univ. of Michigan Press, 2014.

[2] D. G. Long, "Comparison of SeaWinds backscatter imaging algorithms," *IEEE J. Sel. Topics Appl. Earth Observ. Remote Sens.*, vol. 10, no. 3, pp. 2214–2231, May 2017, doi: 10.1109/JSTARS.2016.2626966.

[3] D. S. Early and D. G. Long, "Image reconstruction and enhanced resolution imaging from irregular samples," *IEEE Trans. Geosci. Remote Sens.*, vol. 39, no. 2, pp. 291–302, Feb. 2001, doi: 10.1109/36.905237.

[4] R. D. Lindsley and D. G. Long, "Enhanced-resolution reconstruction of ASCAT backscatter measurements," *IEEE Trans. Geosci. Remote Sens.*, vol. 54, no. 5, pp. 2589–2601, May 2016, doi: 10.1109/TGARS.2015.2503762.

[5] D. G. Long and D. L. Daum, "Spatial resolution enhancement of SSM/I data," *IEEE Trans. Geosci. Remote Sens.*, vol. 36, no. 2, pp. 407–417, Mar. 1998, doi: 10.1109/36.662726.

[6] D. G. Long and M. J. Brodzik, "Optimum image formation for spaceborne microwave radiometer products," *IEEE Trans. Geosci. Remote Sens.*, vol. 54, no. 5, pp. 2763–2779, May 2016, doi: 10.1109/TGARS.2015.2505677.

[7] G. E. Backus and J. F. Gilbert, "Numerical applications of a formalism for geophysical inverse problems," *Geophys. J. Roy. Astron. Soc.*, vol. 13, nos. 1–3, pp. 247–276, Jul. 1967.

[8] G. Backus and J. Gilbert, "The resolving power of gross earth data," *Geophys. J. Roy. Astronomical Soc.*, vol. 16, no. 2, pp. 169–205, 1968.

[9] A. Stogryn, "Estimates of brightness temperatures from scanning radiometer data," *IEEE Trans. Antennas Propag.*, vol. AP-26, no. 5, pp. 720–726, Sep. 1978.

[10] G. A. Poe, "Optimum interpolation of imaging microwave radiometer data," *IEEE Trans. Geosci. Remote Sens.*, vol. 28, no. 5, pp. 800–810, Sep. 1990.

[11] M. R. Farrar and E. A. Smith, "Spatial resolution enhancement of terrestrial features using deconvolved SSM/I microwave brightness temperatures," *IEEE Trans. Geosci. Remote Sens.*, vol. 30, no. 2, pp. 349–355, Mar. 1992.

[12] W. D. Robinson, C. Kummerow, and W. S. Olson, "A technique for enhancing and matching the resolution of microwave measurements from the SSM/I instrument," *IEEE Trans. Geosci. Remote Sens.*, vol. 30, no. 3, pp. 419–429, May 1992.

[13] P. J. Stephens and A. S. Jones, "A computationally efficient discrete Backus–Gilbert footprint-matching algorithm," *IEEE Trans. Geosci. Remote Sens.*, vol. 40, no. 8, pp. 1865–1878, Aug. 2002.

[14] C. T. Swift, M. A. Goodberlet, and S. C. Reising, "Antenna pattern synthesis and deconvolution of microwave radiometer imaging data," in *Proc. IEEE MicroRad*, Feb./Mar. 2006, pp. 216–221.

[15] M. W. Spencer, C. Wu, and D. G. Long, "Improved resolution backscatter measurements with the SeaWinds pencil-beam scatterometer," *IEEE Trans. Geosci. Remote Sens.*, vol. 38, no. 1, pp. 89–104, Jan. 2000, doi: 10.1109/36.823904.

[16] *QuikSCAT Science Data Product User's Manual*, document D-18053, Jet Propulsion Laboratory, 2001.

[17] P. K. Yoho and D. G. Long, "Correlation and covariance of satellite scatterometer measurements," *IEEE Trans. Geosci. Remote Sens.*, vol. 42, no. 6, pp. 1176–1187, Jun. 2004, doi: 10.1109/TGRS.2004.825588.

[18] I. S. Ashcraft and D. G. Long, "The spatial response function of SeaWinds backscatter measurements," in *Proc. SPIE Earth Observ. Syst. VIII*, vol. 5151, W. L. Barnes, Ed. Bellingham, WA, USA: SPIE, Aug. 2003, pp. 609–618, doi: 10.1117/12.506291.

[19] D. G. Long, P. J. Hardin, and P. T. Whiting, "Resolution enhancement of spaceborne scatterometer data," *IEEE Trans. Geosci. Remote Sens.*, vol. 31, no. 3, pp. 700–715, May 1993, doi: 10.1109/36.225536.

[20] B. A. Williams and D. G. Long, "Reconstruction from aperture-filtered samples with application to scatterometer image reconstruction," *IEEE Trans. Geosci. Remote Sens.*, vol. 49, no. 5, pp. 1663–1676, May 2011, doi: 10.1109/TGRS.2010.2086063.

[21] A. M. Plagge, D. C. Vandemark, and D. G. Long, "Coastal validation of ultra-high resolution wind vector retrieval from QuikSCAT in the gulf of maine," *IEEE Geosci. Remote Sens. Lett.*, vol. 6, no. 3, pp. 413–417, Jul. 2009, doi: 10.1109/LGRS.2009.2014852.

[22] R. D. Lindsley, J. R. Blodgett, and D. G. Long, "Analysis and validation of high-resolution wind from ASCAT," *IEEE Trans. Geosci. Remote Sens.*, vol. 54, no. 10, pp. 5699–5711, Oct. 2016, doi: 10.1109/TGRS.2016.2570245.

[23] R. E. Fischer, "Standard deviation of scatterometer measurements from space," *IEEE Trans. Geosci. Electron.*, vol. GE-10, no. 2, pp. 106–113, Apr. 1972.

[24] M. W. Spencer, W.-Y. Tsai, and D. G. Long, "High-resolution measurements with a spaceborne pencil-beam scatterometer using combined range/Doppler discrimination techniques," *IEEE Trans. Geosci. Remote Sens.*, vol. 41, no. 3, pp. 567–581, Mar. 2003, doi: 10.1109/TGRS.2003.809938.

David G. Long (S'80–SM'98–F'08) received the Ph.D. degree in electrical engineering from the University of Southern California, Los Angeles, CA, USA, in 1989.

From 1983 to 1990, he was with the NASA's Jet Propulsion Laboratory, where he was involved in advanced radar remote sensing systems. From 1996 to 1997, he was a Project Engineer in the NASA Scatterometer (NSCAT) Project. He also managed the SCANSCAT Project, the precursor to SeaWinds which was flown in 1999 on QuikSCAT, in 2002 on ADEOS-II, and in 2014 on the International Space Station. He is currently a Professor with the Electrical and Computer Engineering Department, Brigham Young University (BYU), Los Angeles, CA, USA, where he teaches upper division and graduate courses in communications, microwave remote sensing, radar, and signal processing, and the Director of the BYU Center for Remote Sensing. He is the Principle Investigator on several NASA-sponsored research projects in remote sensing. He has authored or co-authored over 400 publications in various areas including signal processing, radar scatterometry, and synthetic aperture radar. His research interests include microwave remote sensing, radar theory, space-based sensing, estimation theory, signal processing, and mesoscale atmospheric dynamics.

Dr. Long was a recipient of the NASA Certificate of Recognition. He is an Associate Editor for IEEE GEOSCIENCE AND REMOTE SENSING LETTERS.